J. Phys. D: Appl. Phys. **18** (1985) 1037–1061. Printed in Great Britain

Dynamics and optics of oil hills and oilscapes

L H Tanner† and M V Berry‡

† 24 Rugby Road, Brighton BN1 6EB, East Sussex, UK

‡ H H Wills Physics Laboratory, University of Bristol, Tyndall Avenue, Bristol BS8 1TL, UK

Received 19 November 1984

Abstract. A pimple or dimple on an otherwise uniform oil film on a flat surface decays under the action of surface tension and viscosity. The process is followed analytically from the Navier–Stokes equation, and by optical experiments employing interferometry and the observation of caustics of refraction. Point or line disturbances give a range of recognisable oil hills and ridges, and the theory predicts their shapes and how these scale with time. If the surface is disturbed in a distributed random way, the interferometric contour map shows a random oilscape. The statistics of the oilscape develop self-similarly by changes in lateral and vertical scales which may be predicted and observed. The theory is well verified for the hills, ridges and oilscapes.

1. Introduction

By spinning oil on to a smooth flat surface, it is easy to produce an optically flat film with a thickness of order 50 μm. This may then be disturbed either by a point disturbance such as a pin-prick, or in a randomly distributed way, as by rolling. The disturbed film then has curvature variations, giving rise to surface tension forces. These restore the film to flatness by producing fluid flow which is resisted by viscosity. At the length scales considered in the paper, gravity forces are negligible by comparison, and no other forces are involved.

The flow resulting from surface tension forces is proportional to rate of change of curvature, so the higher spatial frequencies are very rapidly damped. Although the initial disturbance is unpredictable, the result is that after a short time, recognisable and characteristic forms of disturbance remain, which decay in a predictable manner. Our object is to study the form of such elementary disturbances and to predict their time development.

Similar remarks apply to the randomly disturbed surfaces. Although these are 'rough' in the sense of having random height variations, the rapid decay of high frequencies gives characteristics quite unlike, and much more predictable than, those of rough solid surfaces. The paper shows that the statistics and time development to be expected can be derived by considering a random wave combination, and gives experimental confirmation of the theory.

Earlier work involving optical measurements with oil films has shown how they can be used for skin friction measurement in air flow (Tanner 1981), for viscosity measurement (Tanner 1977) and in the study of rough solid surfaces (Tanner 1982).

0022-3727/85/061037 + 25 $02.25

Studies of the motion of oil droplets on vertical (Tanner 1980) and horizontal (Tanner 1979) surfaces had also been conducted. In the latter case however, the droplets were comparatively large and the initial film thickness either zero or extremely small. By contrast, the present paper deals with disturbances which are small compared with the mean film thickness.

Two experimental techniques have been employed. Firstly, Fizeau interferometry, to obtain contour maps of the disturbed surfaces; and secondly, optical caustics of refraction, interpreted with the aid of catastrophe theory (as reviewed by Berry and Upstill 1980), to study the superposition of oil hills and the temporal scaling of oilscapes.

2. Theory

2.1. Surface profile equation

Let $\boldsymbol{r} = (x, y)$ be coordinates in the plane of the undisturbed film's free surface, and let $\zeta = z(\boldsymbol{r}, t)$ be the profile of the disturbed surface, measured as the deviation from this plane. An equation for $z(\boldsymbol{r}, t)$ will now be obtained under the following assumptions: the length scales are small enough for gravity to be neglected; z is sufficiently small in comparison with h, and sufficiently slowly varying, for the total curvature to be approximated by $\nabla^2 z$; the ζ component of the flow velocity $\boldsymbol{u}(\boldsymbol{r}, \zeta, t)$ is negligible; $\boldsymbol{u}$ is small enough for fluid inertia to be negligible; and the pressure p is independent of depth ζ.

The equation for $z(\boldsymbol{r}, t)$ involves three physical principles. Firstly, *Laplace's equation* relates p to the surface curvature by

$$p(\boldsymbol{r}, t) = -\sigma \nabla^2 z(\boldsymbol{r}, t) \tag{1}$$

where σ is the surface tension. Secondly, the *Navier–Stokes equation* relates p to the velocity variations by

$$\nabla p(\boldsymbol{r}, t) = \mu \nabla^2 \boldsymbol{u}(\boldsymbol{r}, \zeta, t) \tag{2}$$

where μ is the viscosity. Because the film is thin, $\boldsymbol{u}$ varies most rapidly in the ζ direction so that ∇^2 can be replaced by $\partial^2/\partial\zeta^2$. Thus the Navier–Stokes equation can be integrated, using the boundary condition that $\boldsymbol{u} = 0$ on the fixed surface $\zeta = -h$, to give an expression for the mean flow velocity $\boldsymbol{v}(\boldsymbol{r}, t)$, namely

$$\boldsymbol{v}(\boldsymbol{r}, t) \equiv \frac{1}{h}\int_{-h}^{0} \mathrm{d}\zeta\, \boldsymbol{u}(\boldsymbol{r}, \zeta, t) = -\frac{h^2}{3\mu}\nabla p(\boldsymbol{r}, t). \tag{3}$$

Thirdly, the *continuity equation* relates the change in height of fluid columns to the outflow through their surface, by

$$-\frac{\partial z}{\partial t}(\boldsymbol{r}, t) \equiv h\nabla \cdot \boldsymbol{v}(\boldsymbol{r}, t). \tag{4}$$

Substitution of equation (3) and then (1) into equation (4) now shows that the surface profile satisfies the biharmonic diffusion equation

$$\frac{\partial z}{\partial t}(\boldsymbol{r}, t) = -\frac{h^4}{4\tau}\nabla^4 z(\boldsymbol{r}, t) \tag{5}$$

where

$$\tau \equiv 3\mu h/4\sigma.$$

The general solution is a superposition of decaying plane waves with wave-vectors $\boldsymbol{s} = (s_x, s_y)$ and coefficients $c(\boldsymbol{s})$:

$$z(\boldsymbol{r}, t) = \iint \mathrm{d}\boldsymbol{s}\, c(\boldsymbol{s}) \exp(\mathrm{i}\boldsymbol{s} \cdot \boldsymbol{r} - h^4 s^4 t/4\tau). \tag{6}$$

It is clear that $c(\boldsymbol{s})$ is the (spatial) spectrum of the surface profile at the initial instant $t = 0$. As time proceeds, the short wavelength (large $|\boldsymbol{s}|$) components are damped by the exponential time factor. For broad-band initial profiles this can lead to oil hills, oil ridges and oilscapes whose characteristic lengths grow as $t^{1/4}$. In the next three sections, surfaces will be presented where this growth corresponds to self-similarity, with surfaces at different times related by a scaling transformation.

2.2. Oil hills in three dimensions

For the spectrum we taken the simplest isotropic integral powers, namely

$$c(\boldsymbol{s}) = (s_x + \mathrm{i}s_y)^k. \tag{7}$$

Then in polar coordinates $\boldsymbol{r} = (r, \theta)$, $\boldsymbol{s} = (s, \theta_s)$ the integration over θ_s in equation (6) gives a Bessel function (Gradshteyn and Ryzhik 1965) written in the form

$$z_k(\boldsymbol{r}, t) = ah\left(\frac{\tau}{t}\right)^{(k+2)/4} \cos k\theta\, Z_k(\rho) \tag{8}$$

where ρ is the dimensionless radius parameter

$$\rho \equiv \frac{r}{h}\left(\frac{\tau}{t}\right)^{1/4} \tag{9}$$

a is a dimensionless constant and the functionx $Z_k(\rho)$ are

$$Z_k(\rho) \equiv \int_0^\infty \mathrm{d}\sigma\, \sigma^{k+1} \exp(-\sigma^4/4) J_k(\rho\sigma). \tag{10}$$

At $t = 0$ these different k-hills are all singular and correspond to pin-pricks with different azimuthal structures, localised at $r = 0$. They shrink vertically and expand laterally in self-similar fashion with profiles $Z_k(\rho)$, the first four of which are illustrated in figure 1(*a*). The zero-order hill represents a disturbance whose volume is constant in time and given by

$$\int_0^\infty \mathrm{d}r \int_0^{2\pi} \mathrm{d}\theta\, r z_k(\boldsymbol{r}, t) = 2\pi a h^3. \tag{11}$$

The hills $k > 0$ have zero volume.

The integral over Bessel functions in $Z_k(\rho)$ as defined by equation (10) is not expressible in closed form in terms of standard functions, but its structure can be elucidated by means of approximations as explained in appendix 1.

2.3. Oil ridges in two dimensions

For the spectrum we now take the simplest integral powers corresponding to wave-

vectors in the x direction, namely

$$c(\boldsymbol{s}) = (\mathrm{i}s_x)^j \delta(s_y) \tag{12}$$

where δ denotes the Dirac function. From equation (6) the evolving profiles can be written as

$$z_j(x, t) = ah\left(\frac{\tau}{t}\right)^{(j+1)/4} Z_j(\xi) \tag{13}$$

where ξ is the dimensionless distance parameter

$$\xi \equiv \frac{x}{h}\left(\frac{\tau}{t}\right)^{1/4} \tag{14}$$

a is a dimensionless constant and the functions $Z_j(\xi)$ are

$$Z_j(\xi) = \mathrm{Re}\int_0^\infty \mathrm{d}\sigma(\mathrm{i}\sigma)^j \exp(\mathrm{i}\sigma\xi)\exp(-\sigma^4/4)$$

$$= \frac{\mathrm{d}^j}{\mathrm{d}\xi^j}\int_0^\infty \mathrm{d}\sigma \cos(\sigma\xi)\exp(-\sigma^4/4). \tag{15}$$

At $t = 0$ these different j-ridges are all singular and correspond to derivatives of δ functions localised at $x = 0$. They shrink vertically and expand laterally in self-similar

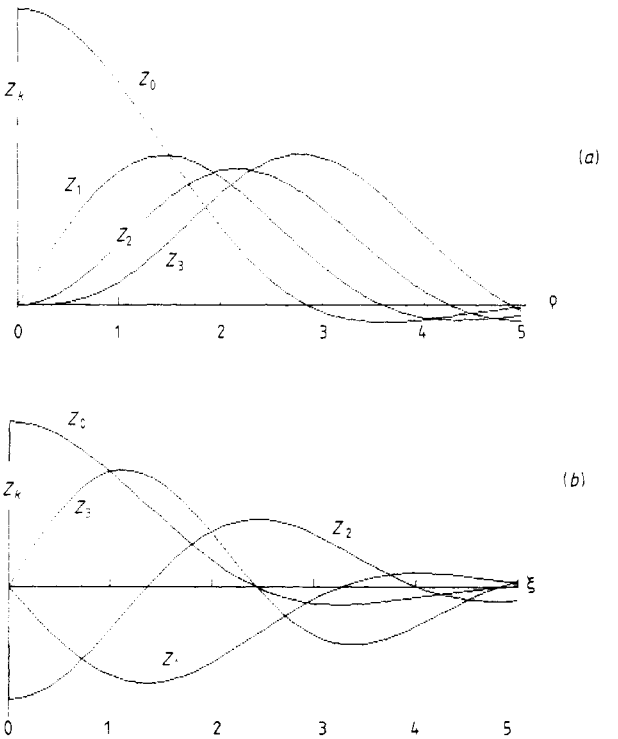

Figure 1. Theoretical oil hill profiles for $k = 0$ to 3, (a) three dimensions, (b) two dimensions.

fashion with profiles $Z_j(\xi)$, the first four of which are illustrated in figure 1(*b*). The zero-order ridge represents a disturbance whose volume per unit length is constant in time and given by

$$\int_{-\infty}^{\infty} \mathrm{d}x\, z_0(x, t) = \pi a h^2. \tag{16}$$

The ridges $j > 0$ have zero volume per unit length.

Approximations for the integrals (15) defining $Z_k(\xi)$ are given in Appendix 2.

2.4. *Random oilscapes*

In the fundamental solution (6), let the phases of the coefficients $c(s)$ be uncorrelated for different s. Then the initial surface profile corresponds to an extended disturbance in the form of a Gaussian random function (Longuet-Higgins 1957a, b) of $\boldsymbol{r}$, with spectrum proportional to $|c(s)|^2$. Denoting the subsequent spectrum by $P(s, t)$, we find from equation (6) that

$$P(s, t) = P(s, 0) \exp(-2h^4 s^4 t/4\tau). \tag{17}$$

It is clear that any particular statistical structure, corresponding to a feature of $P(s, 0)$ on a scale $s_0 \equiv r_0^{-1}$, will be damped out for times

$$t \gtrsim \tau(r_0/h)^{1/4}.$$

But if $P(s, 0)$ is a power-law its lack of features enables the surface to remain statistically self-similar, with different quantities scaling differently with t in a manner soon to be described.

Attention will be restricted to surfaces with statistical isotropy, and the power-law spectra will be written as

$$P(s, 0) = ah^4(sh)^{\mu} \tag{18}$$

where a is a dimensionless constant. The most familiar of these μ-scapes are fractals (Mandelbrot 1982), for which $-4 < \mu < -2$, corresponding to non-differentiable surfaces with Hausdorff dimension $4 + \mu/2$ lying between 2 and 3. However, as we shall see in § 3.4, experiments indicate that oilscapes are not fractals, and strongly suggest $\mu \approx 2$. If extrapolated to $s = \infty$ this would represent an initial profile that is not merely non-differentiable but also discontinuous—and even more severely so than the white-noise case $\mu = 0$. But of course there must be a value $s = s_{\max}$ above which equation (18) does not apply and $P(s, 0)$ falls to zero; the factor $\exp(-s_{\max}^4 t)$ ensures that there will be a corresponding time (which is of the order of milliseconds if $s_{\max} \sim 2\pi/h$) after which departures from equation (18) have no effect. We shall keep the general form (18) in order to show which statistics evolve in a manner that depends on μ, and which do not.

In describing the statistics, angle brackets will be used to denote averages over an ensemble of surfaces (distinguished by different sets of phases of the coefficient $c(s)$) or, equivalently, averages over all positions on a given surface. Thus the *autocovariance* is defined as the average $\langle z(\boldsymbol{r}, t) z(\boldsymbol{r}', t)\rangle$ and given (Longuet-Higgins, 1957a, b) by the Fourier transform of $P(s, t)$:

$$\langle z(\boldsymbol{r}, t) z(\boldsymbol{r}', t)\rangle = \iint \mathbf{ds}\, P(s, t) \exp[\mathrm{i}\mathbf{s} \cdot (\boldsymbol{r} - \boldsymbol{r}')]. \tag{19}$$

From this, together with equations (17) and (18), it follows that the *mean square height* is

$$\langle z^2(t)\rangle = a\pi h^2 2^{(\mu-2)/4}\Gamma\left(\frac{\mu+2}{4}\right)\left(\frac{\tau}{t}\right)^{(\mu+2)/4} \tag{20}$$

showing that the heights of the different μ-scapes decay differently. In particular, for $\mu = 2$ the heights decay as $t^{-1/2}$.

On the other hand, the *autocorrelation* is

$$C(\boldsymbol{r}-\boldsymbol{r}', t) \equiv \frac{\langle z(\boldsymbol{r}, t)z(\boldsymbol{r}', t)\rangle}{\langle z^2(t)\rangle} = \frac{\int_0^\infty \mathrm{d}\sigma\, \sigma^{\mu+1}J_0(\rho\sigma)\exp(-\sigma^4/2)}{\int_0^\infty \mathrm{d}\sigma\, \sigma^{\mu+1}\exp(-\sigma^4/2)} \tag{21}$$

where

$$\rho \equiv \left|\frac{\boldsymbol{r}-\boldsymbol{r}'}{h}\right|\left(\frac{\tau}{t}\right)^{1/4}. \tag{22}$$

The dependence on ρ shows that the correlations are similar at different times and scale laterally as $t^{1/4}$, i.e. independently of μ. The invariant form of the autocorrelation does depend on μ, but all the functions fall from unity at $\rho = 0$ in an initially approximately Gaussian fashion, with exponentially oscillating decay as $\rho \to \infty$.

The *density of extrema* (maxima and minima) (Longuet-Higgins 1957a, b) is

$$D = \frac{1}{4\pi\sqrt{3}}\frac{\iint \mathbf{ds}\, s^4P(s, t)}{\iint \mathbf{ds}\, s^2P(s, t)} = \sqrt{\frac{2}{3}}\frac{\Gamma[(\mu+6)/4]}{4\pi h^2\Gamma[(\mu/4)+1]}\left(\frac{\tau}{t}\right)^{1/2} \tag{23}$$

and thus decreases in the same way for all the μ-scapes. The mechanism of decrease is coalescence of extrema with saddles, detectable optically either by direct observation of the interferogram or by far-field caustic lines sweeping through the forward direction.

Scaling laws for derivatives of z can be determined from the fact that each derivative corresponds (cf. equation (6)) to an extra factor s in the integrals over $P(s, t)$. Thus the *mean square gradient* is

$$\begin{aligned}\langle|\nabla z(t)|^2\rangle &= \iint \mathbf{ds}\, s^2P(s, t)\\ &= a\pi 2^{\mu/4}\Gamma\left(\frac{\mu+1}{4}\right)\left(\frac{\tau}{t}\right)^{(\mu/4)+1}\end{aligned} \tag{24}$$

showing that for $\mu = 2$ gradients decay as $t^{-3/4}$. Similarly, the *mean square total curvature* is

$$\begin{aligned}\langle(\nabla^2 z(t))^2\rangle &= \iint \mathrm{d}s\, s^4P(s, t)\\ &= \frac{a\pi 2^{(\mu+2)/4}}{h^2}\Gamma\left(\frac{\mu+6}{4}\right)\left(\frac{\tau}{t}\right)^{(\mu+6)/4}\end{aligned} \tag{25}$$

showing that for $\mu = 2$ curvatures decay as t^{-1}, and radii of curvature increase linearly.

3. Experimental methods and results

3.1. Methods

The oil films were made by placing one or two drops of silicone oil, kinematic viscosity

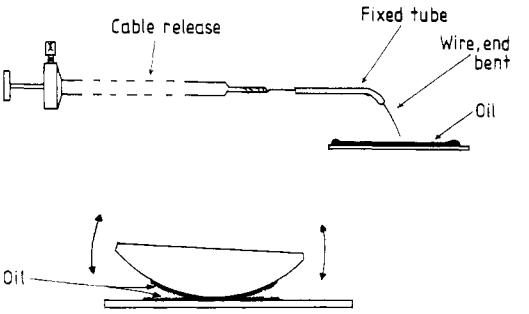

Figure 2. Methods of formation of (*a*) isolated oil hills, (*b*) random oilscapes.

0.0125 $m^2 s^{-1}$ or 0.1 $m^2 s^{-1}$, at the centre of a slide, then spinning with an electric hand drill, at 50 rev s^{-1} for about 15 s. This gives a film which, except near its edges, has perfectly uniform thickness.

The point disturbances were made by pin-pricks, using a fine wire controlled by camera cable release, figure 2(*a*). The operation can be seen through the camera viewfinder, and timing started when the wire leaves the surface.

The random surfaces were made by rolling with a cylindrical lens, figure 2(*b*).

For the interferometric contour maps of the oil films, a Fizeau interferometer was arranged as in figure 3(*a*). Ideally, the slide should have a partially reflecting top surface, with reflection from the back prevented by grinding. Omission of the partially reflective

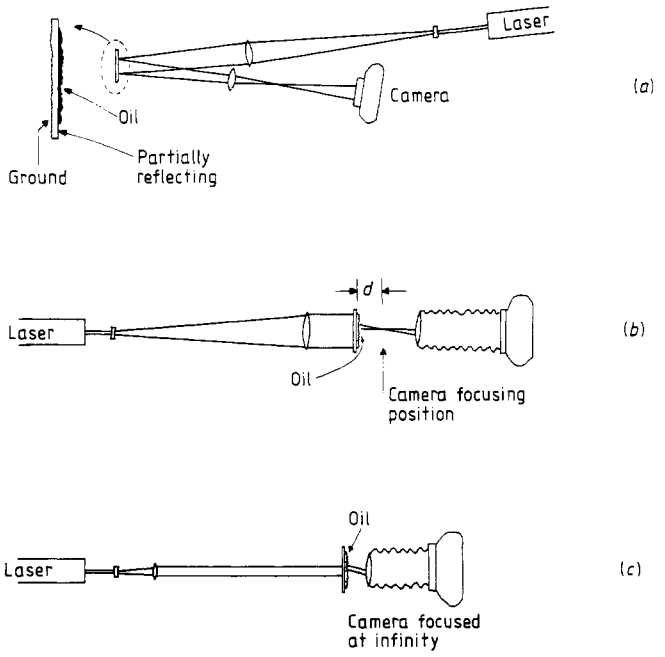

Figure 3. Optical arrangement for (*a*) Fizeau interferometry of oil hills and oilscapes, (*b*) near-field and (*c*) far-field caustics.

coating gives some loss of fringe contrast. A further alternative is the use of the reflection from the back surface of a plain slide, if the slide has sufficiently uniform thickness. The figures include examples of all of these techniques.

With helium–neon laser light of wavelength 0.633 μm and oil of refractive index 1.4, the contour interval is 0.226 μm.

For the caustics, the arrangement of figure 3(*b*) for the near field and figure 3(*c*) for the far field was used.

3.2. Point disturbances in three dimensions

Figure 4(*a*) shows an attempt to produce the zero-order hill z_0 of § 2.2. This was done by having a slight excess of oil on the end of the wire of figure 2(*a*), which was thus deposited on the surface. Figure 4(*b*) shows a comparison between the experimental profile, obtained by measuring microscope from the interferogram, and the computed theoretical curve, showing nearly perfect agreement.

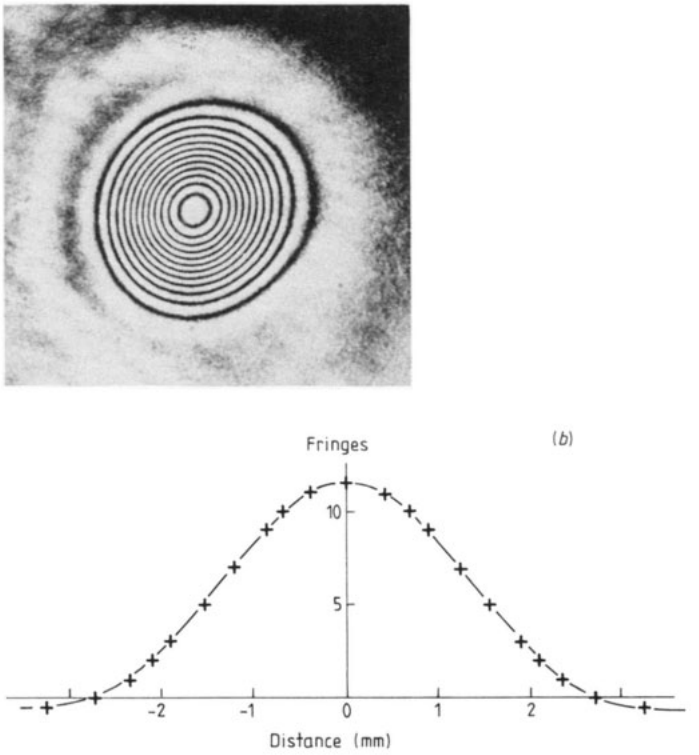

Figure 4.(*a*) Interferogram of zero-order hill, (*b*) profile comparison: line is theoretical, points experimental.

With no excess of oil on the wire, the usual result of the pin-prick is either a combination of z_0 with z_1, or a combination of two z_0 profiles with different scales, involving little or no volume change to the film. Figure 5(*a*) may be regarded as a combination of z_0 and z_1, of the form

$$z = a_0 z_0(x/L) + a_1 z_1(x/L).$$

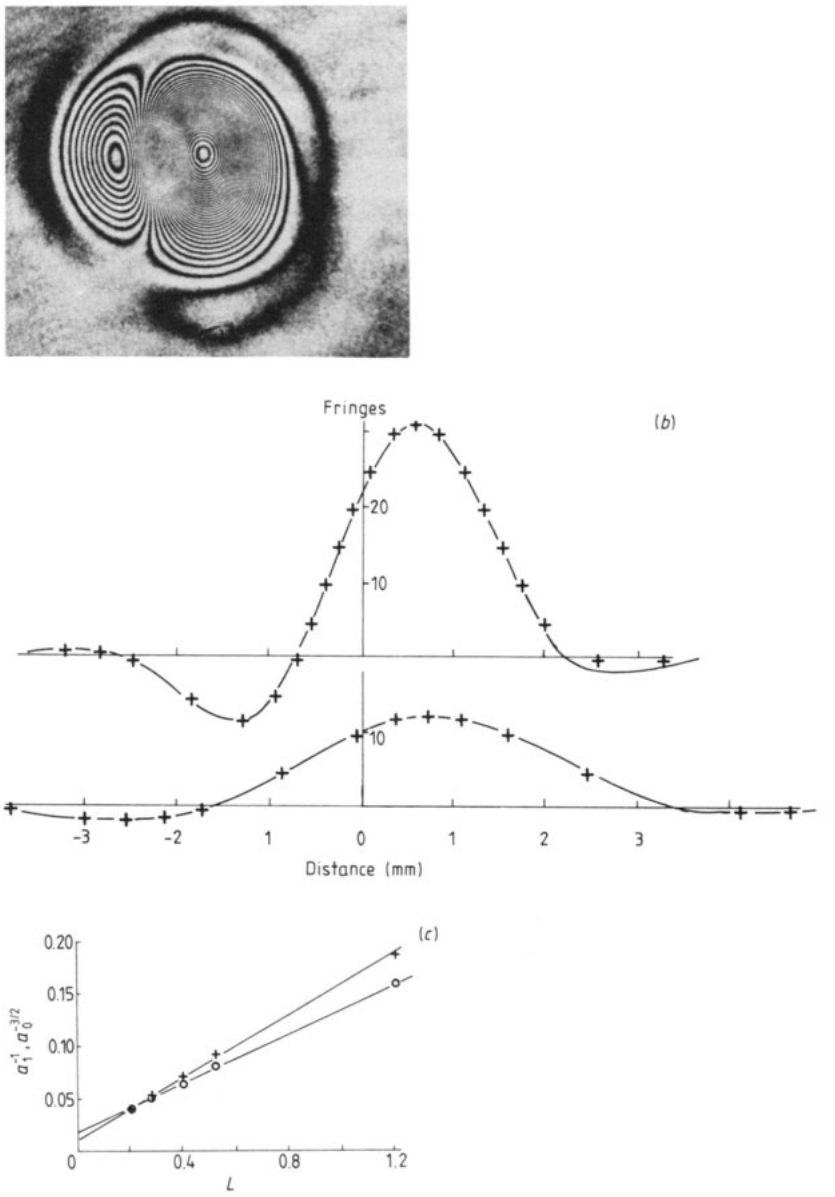

Figure 5. (*a*) Interferogram of combination zero plus first-order hill; (*b*) profile comparison for two time stages: lines theoretical, points experimental; (*c*) (+) a_1^{-1} and (○) $a_0^{-3/2} \times 5$ versus L^3 for five time stages of the same hill.

The experimental profiles along the line of symmetry were measured, and the best fit obtained by adjustment of a_0, a_1 and L for each. The result corresponding to figure 5(*a*), together with one for a later time stage, is shown in figure 5(*b*). It is also possible to compute the theoretical contour maps using the same values of a_0, a_1 and L, and these show that the agreement extends over the whole area and is not confined to that of the centre-line profiles shown here.

The change in shape of the profile with time results from the fact that, since the heights vary as $t^{-(k+2)/4}$ the z_1 part of the hill decays faster than the z_0. Because L increases as $t^{1/4}$ the relation between a_1, a_0 and L is such that a_1^{-1} should be proportional to $a_0^{-3/2}$ and to L^3. Figure 5(*c*) shows a_1^{-1} and $a_0^{-3/2}$ versus L^3 and confirms the linear relationships. The fact that the lines do not pass through the origin is not surprising since, as already pointed out, in the initial stages the heights and slopes involved in the hill will lie outside the range of the theory.

Figure 6(*a*) shows a hill which must be regarded as a combination of a wide negative z_0 hill with a narrower positive one slightly offset from its centre. It is easy to visualise how such a hollow with central peak would form when a wire is withdrawn from the surface.

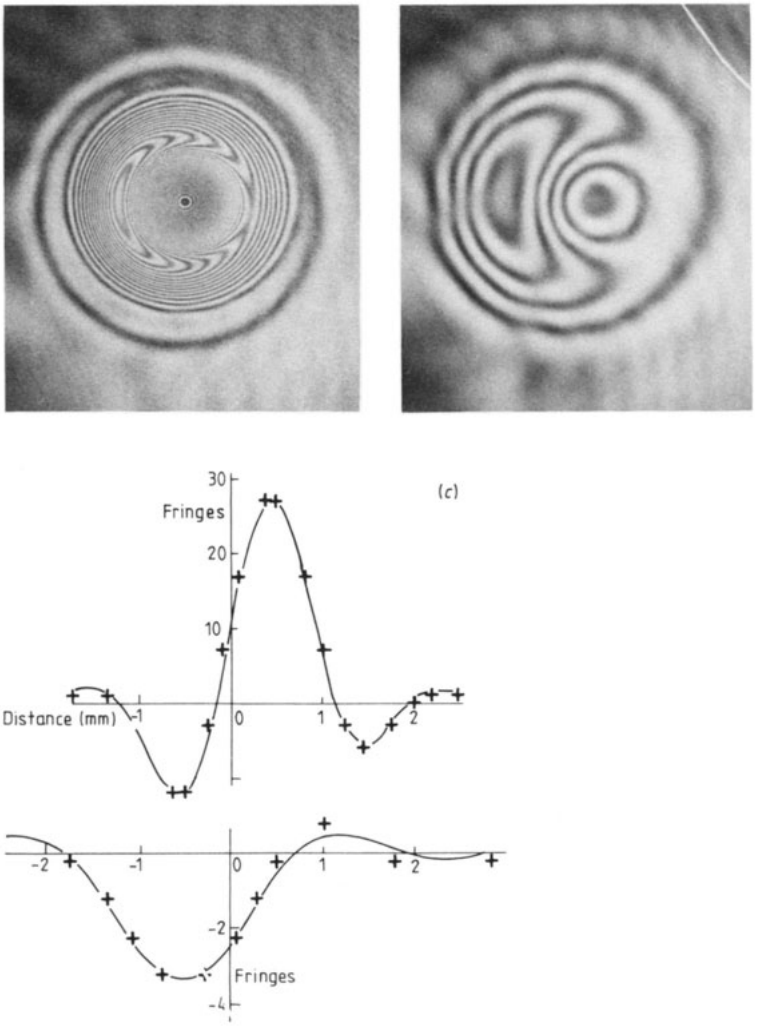

Figure 6. (*a*), (*b*) Interferograms showing two time stages of a hill which is a combination of one wide and one narrow zero-order hill. (*c*) Profile comparison: line theoretical, points experimental. The fringes of the peak in (*a*), not resolved on the print, are clearly resolved by microscope.

The z_0 hill has the form $z = a_0 Z_0(\rho)$ where

$$\rho = \left(\frac{r}{h}\right)\left(\frac{3\mu h}{4\sigma t}\right)^{1/4}.$$

To obtain two hills, one wide and one narrow, one must imagine the wider one having been formed at an earlier time. If hill B is formed at time $t = -\tau$ and hill A at $t = 0$, then at a later time we should have

$$z = \frac{at_0}{t^{1/2}} Z_0\left(\frac{cr}{t^{1/4}}\right) + \frac{bt_0}{(t+\tau)^{1/2}} Z_0\left(\frac{cr}{(t+\tau)^{1/4}}\right).$$

The result is that the narrower and more recently formed hill A decays more rapidly, while the ratio of the widths of the hills tends towards unity. Figure 6(b) shows a later time stage for the same hill, showing the very great change in appearance with the narrower hill having almost disappeared. Figure 6(c) shows the measured profiles and fitted theoretical curves of the form

$$z = aZ_0\left(\frac{x}{A}\right) + bZ_0\left(\frac{x-d}{B}\right).$$

Using suffix 1 for the first and 2 for the second time stage, we should expect to find

$$\left(\frac{a_2}{a_1}\right) = \left(\frac{A_1}{A_2}\right)^2 = \left(\frac{t_1}{t_2}\right)^{1/2} \qquad \left(\frac{b_2}{b_1}\right) = \left(\frac{B_1}{B_2}\right)^2 = \left(\frac{t_1+\tau}{t_2+\tau}\right)^{1/2}.$$

The results actually obtained for these ratios are given below, together with the initial and final width ratios A_1/B_1 and A_2/B_2. (τ/t_1 was estimated from b_2/b_1 and $(B_1/B_2)^2$.)

$(t_1/t_2)^{1/2}$	a_2/a_1	$(A_1/A_2)^2$	b_2/b_1	$(B_1/B_2)^2$	A_1/B_1	A_2/B_2	τ/t_1
0.363	0.341	0.339	0.578	0.534	0.75	0.94	1.95

This shows that there is good agreement between the theoretically expected development of the profile and that observed experimentally, and confirms that the hill can be treated as sum of two elementary z_0 hills.

Figure 7(a, b, c) shows three examples of the far-field caustics produced by the oil hills, obtained as shown in figure 3(c). These hills were produced in the same way as that of figure 5(a), and are almost certainly similar to it in consisting of a combination of Z_0 and Z_1. The theory of these caustics is given in Appendix 3. With pure Z_1, the caustic should show the singular 'corner' section of a hyperbolic umbilic catastrophe with an angle of 60°: figure 7(a) is close to this condition with an angle of 55° in fair agreement with theory. Figures 7(b, c) show the development of the caustic as the proportion of Z_0 relative to Z_1 increases. For comparison figures 7(d, e, f) show the theoretical forms of the caustics, obtained as explained in Appendix 3 by using a Gaussian profile $(x + a)$ $\exp[-(x^2 + y^2)/2]$ rather than the true Bessel–integral function.

It is possible to compute the caustics for the true $(Z_1 + aZ_0)$ combination, and while these show (over this range of a) no topographical differences from the Gaussian, there is a difference of proportion, resulting from the different maximum to minimum slope ratios of Z_1 and of $x \exp -x^2/2$: the ratio l/L in figure 7(d) is 0.446, whereas for the true $(Z_1 + aZ_0)$ combination its value is 0.572. It was at first sight surprising to note that the

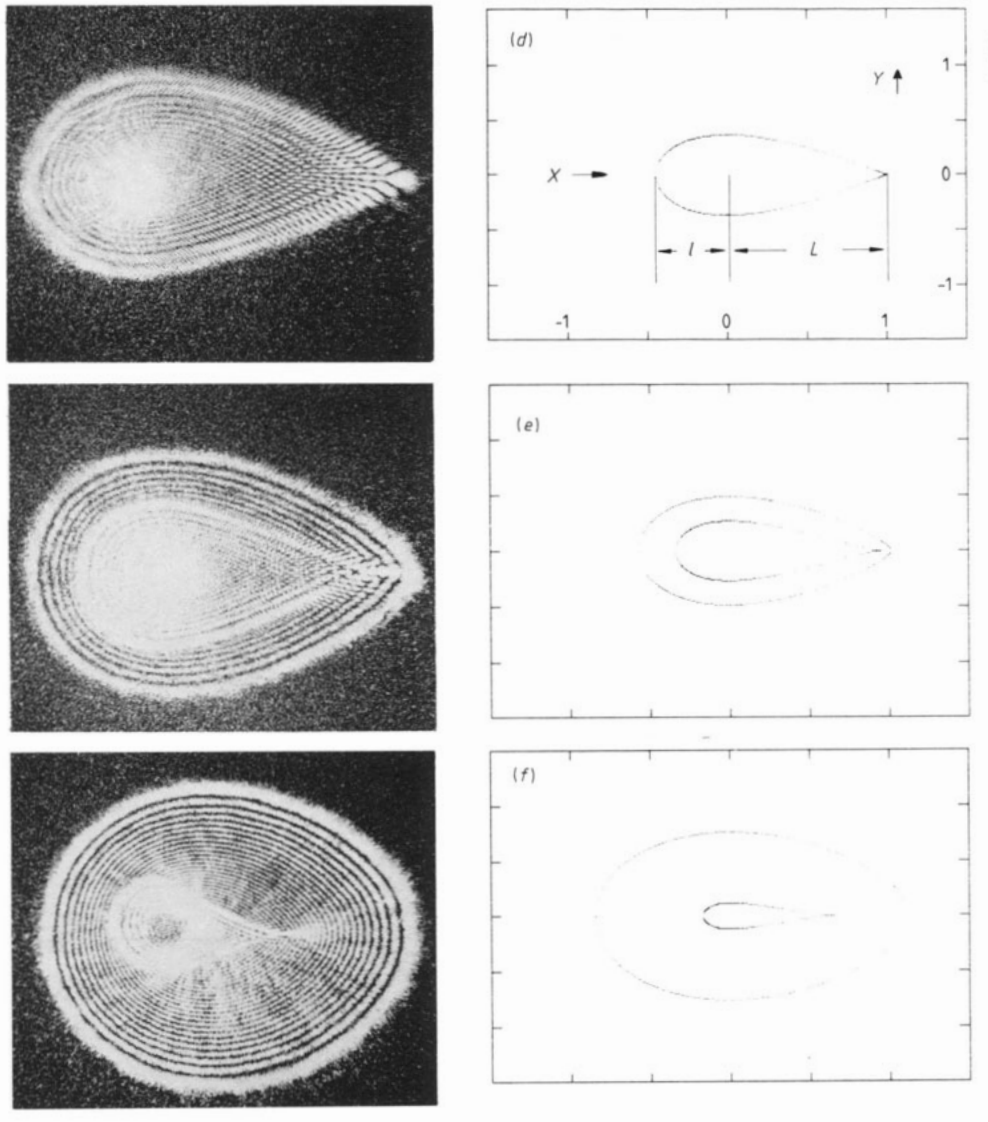

Figure 7. (*a*), (*b*), (*c*) Far-field caustics of combined first and zero order hills. (*d*), (*e*), (*f*) Theoretical forms for Gaussian profile (note the different horizontal and vertical scales: the actual corner angle in (*d*) is 60°).

experimental values obtained from the caustics lie closer to the Gaussian than to the Z_1 value. However, it seems conceivable that in their early stages the oil hills may be smoothly asymptotic to the mean level, like the Gaussian, rather than oscillatory, like the Bessel integral. Their form would change towards that of the Bessel integral. The change can be followed by computation, using the representation of the Gaussian explained in Appendix 1 (equation A1.9). It appears that the initial stages of profile change are rapid, although the full relative amplitude of the outer waves is approached asymptoticaly and very slowly. As an indication of the earlier part of the development,

the first minimum of the wave system reaches half of its final relative depth when the hill height has fallen to 0.37 of its initial value.

3.3. Two-dimensional disturbances

The two-dimensional zero-order oil hill of § 2.3 may be produced in two ways. With the most viscous oil it is possible to catch a very fine falling thread of the oil by moving a slide, already coated with a spun film, across its path. Alternatively, a fine nylon thread, laid across the surface and quickly raised from it, gives the same effect as a pin-prick in three dimensions, producing either the zero order or sometimes a more complex result.

Figure 8(*a*) shows an interferogram of a hill produced by raising a thread, while figure 8(*b*) compares the experimental and theoretical profiles, showing that the agreement is as good as with the corresponding three-dimensional result of figure 4(*b*). Three profiles from interferograms taken at different times were measured and show close similarity and show the expected linear variation with time of w^4 and h^{-4}, where w and h are the width and height of the profile.

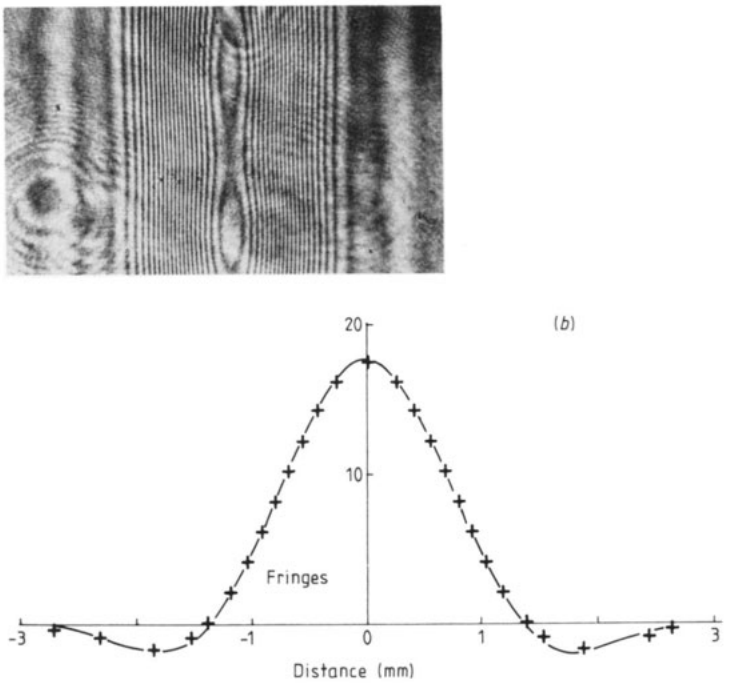

Figure 8. (*a*) Interferogram of two-dimensional zero-order ridge (*b*) Profile comparison; line theoretical, points experimental.

A further interesting method which produces an approximately two-dimensional hill is shown in figure 9(*a*). The oil film here is falling under gravity, a technique which gives a parabolic film thickness variation (Jeffreys 1930, Tanner and Blows 1976), which may be seen in the outer parts of the interferogram. In the path of the flowing film a point obstacle (a speck of araldite) is placed, giving rise to the pattern shown. The 'wake' is a roughly two-dimensional hill. Figure 9(*b*) shows a profile across the wake, at a point well

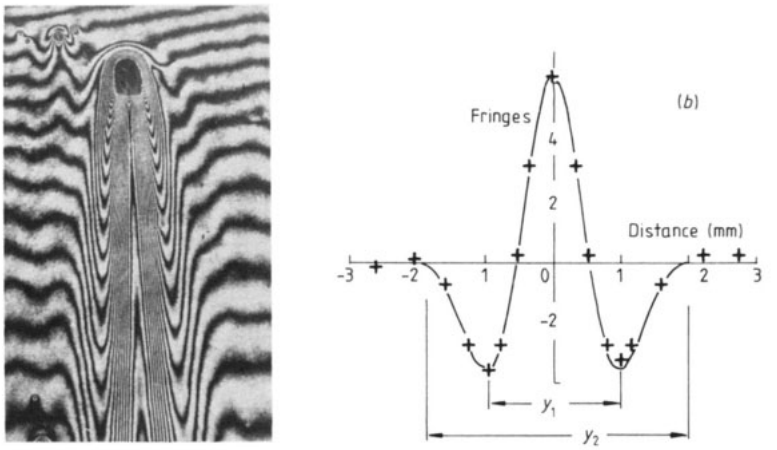

Figure 9. (*a*) Interferogram showing gravity flow past point obstacle. (*b*) Profile comparison for wake.

behind the obstacle, and compares it with a combination of two of the zero-order profiles of width ratio 2:1.

A theoretical prediction of the wake width variation may be attempted. Take x-axis in the flow direction, y across it. The film thickness h in the undisturbed flow is given by $h^2 = (\nu x/(gt)$, and the characteristic velocity (Tanner and Blows 1976), is gh^2/ν. Considering a given position x, if the interferogram is taken at time t_1, then the time taken to travel from the obstacle at x_0 to x along the characteristic is $[(x - x_0)/x]t_1$. This is the development time for the wake at this position. The parameter ξ of para. 2 is

$$\xi = \frac{y}{h}\left(\frac{3}{4}\frac{\mu h}{\sigma t}\right)^{1/4}$$

so for a given ξ, y is proportional to $(h^3 t)^{1/4}$, and hence to

$$\left(\frac{x}{t_1}\right)^{3/8}\left(\frac{(x - x_0)}{x}t_1\right)^{1/4}$$

or to $x^{1/8}(x - x_0)^{1/4}$.

Wake widths y_1 and y_2 as indicated on figure 9(*b*) were measured from figure 9(*a*).

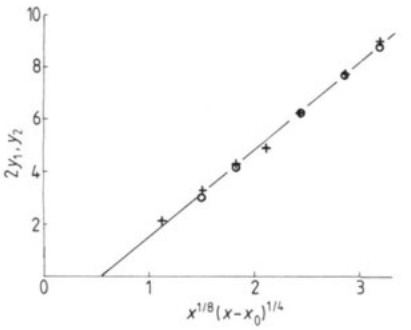

Figure 10. Wake widths y_2 and $2y_1$ versus $x^{1/8}(x - x_0)^{1/4}$ from figure 9(*a*).

Figure 10 shows the results plotted against $x^{1/8}(x - x_0)^{1/4}$, showing an approximately linear variation, with $y_2 = 2y_1$.

3.4. Random disturbances

If a drop of highly viscous oil is squeezed between two glass slides, and the slides are pulled rapidly apart, the disturbed oil film consists of very thin flat areas separated by oil ridges having a dendritic formation. This may be 'frozen' by using, in place of oil, a solution of perspex in dichloromethane. When the slides are separated the solvent rapidly evaporates, the surface solidifies and spreading is prevented. Figure 11 shows an interferogram of the perspex dendrites.

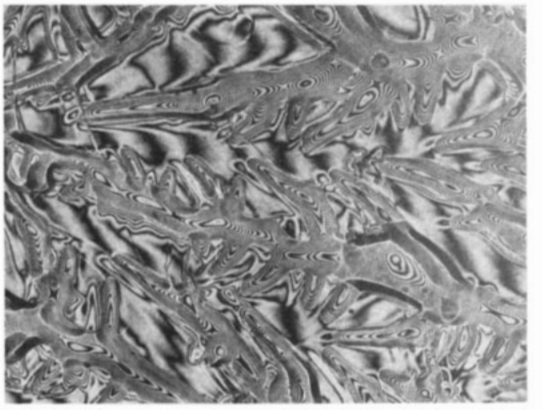

Figure 11. Interferogram of perspex dendrites.

When the disturbed oil film is produced by rolling, a similar dendritic structure results if the oil film is extremely thin compared to the roller radius, and if a single pass of the roller is used. With a larger film thickness to roller radius ratio, and particularly if multi-pass rolling is used, the dendritic effect disappears and the result is more isotropic, with less extreme thickness variations. The effect of surface tension on a disturbed film of this type is then to reduce rapidly the higher spatial frequencies, and the oilscape tends towards an isotropic Gaussian random form as described in § 2.4.

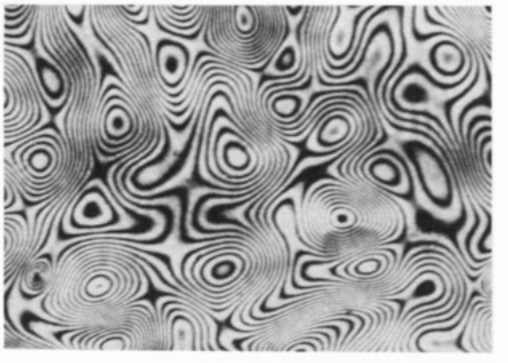

Figure 12. Interferogram showing typical random oilscape.

Figure 12 shows a typical interferogram of such an oilscape, showing the isotropy. The figure suggests a band-limited spatial frequency range, with the rather sharp upper frequency cut-off which would be an expected result of the surface tension, and also with very little low-frequency content. As time passes, the height variations are reduced and the lateral scale increases, but if the appropriate scaling factors are taken into account there is observed to be statistical similarity between any two instantaneous views of the oilscape, and also between any two different oilscapes.

The near-field caustics formed by a laser beam passing through the oilscape as in figure 3(b) are of interest. Figure 13(a, b) shows the caustics at an early stage of development (4 min after the film formation), for distances $d = +12.5$ and -12.5 mm.

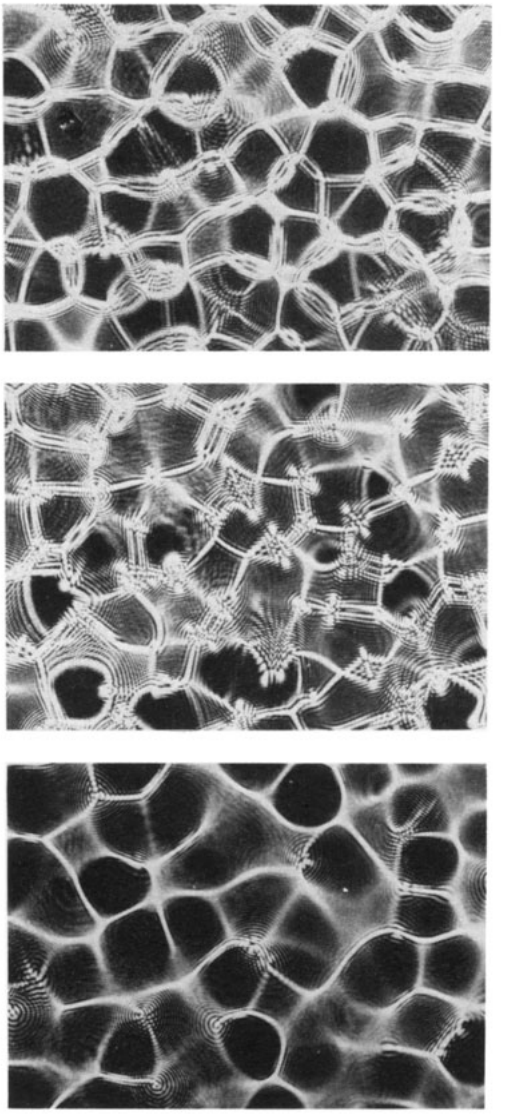

Figure 13. (a), (b), (c) Near-field caustics of oilscapes. (a) $t = 4$ min, $d = +12.5$ mm (see figure 3(b)); (b) $t = 4$ min $d = -12.5$ mm; (c) $t = 8$ min, $d = +12.5$ mm.

The difference between the two caustics shows that there is an asymmetry between the hills and valleys of the oilscapes: the valleys focus more strongly than the hills, indicating that their curvatures are greater. This focal difference can also be observed directly. It is a nonlinear effect which can however be understood on the basis of the linear profile equation (5), as follows: the rate at which initial irregularities are ironed out is proportional to h^3 and is thus greater for the hills, where h is larger, so that large initial curvatures survive longer in the valleys. (It can be shown that the curvature difference between hills and valleys is proportional to $(z_{max}/h)^2$, where z_{max} is the height of the hills.) At a later stage, such as that shown in figure 12, nonlinearity is negligible and no asymmetry is apparent.

Figure 13(*c*) shows the caustic for $d = +12.5$ mm at $t = 8$ min. The regular 'chicken-wire' pattern is readily recognizable and repeatable and is characterised by high intensity concentration and contrast. In terms of the caustic surface in three-dimensional space, chicken-wire corresponds to a plane section parallel to the film, at the distance of smallest local mean radius of curvature; this distance is fairly well-defined because of the band-limited nature of the spectrum. The lines of the chicken-wire are cuspidal creases (ribs—Berry and Upstill 1980) in the caustic surface, which at this distance are almost parallel to the film because they are closest to it. Chicken-wire may be used both to study lateral scale change and, by regarding it as an 'average focal position', to study time variation of curvature.

For the lateral scale variation, the distance d was increased so as to keep the chicken-wire in focus, and a set of photographs taken at times increasing by factors of 2. By imaging one photograph on to another with factor 2 magnification, it was then possible to check that a time increase of 16 gives a scale increase of 2, in agreement with the $t^{1/4}$ variation predicted in § 2.4 (cf. equations (21) and (22)).

A more quantitative measure of the lateral scale may be obtained from the oilscape interferograms. A set of interferograms was taken, with time increasing by a factor $\sqrt{2}$ between them. The negatives were projected and the number of extrema within a given area counted. For an isotropic Gaussian surface the extrema density as given by equation (23) scales as $t^{-1/2}$, and this is independent of the oilscape exponent μ introduced in equation (18). Figure 14 shows the number N against $t^{-1/2}$ and confirms the expected linear variation. The failure of the line to pass through the origin is to be expected, since extrema involving level differences less than about $\frac{1}{4}$ fringe are likely to be uncounted,

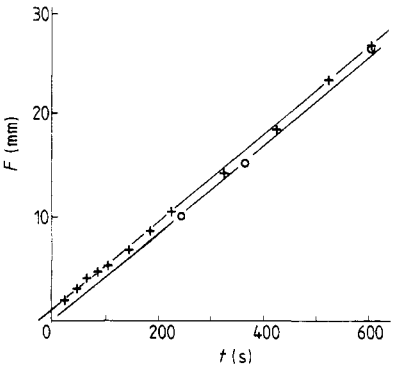

Figure 14. Focal distance versus time for 'chicken-wire' caustic. For the circled points both scales are multiplied by 5.

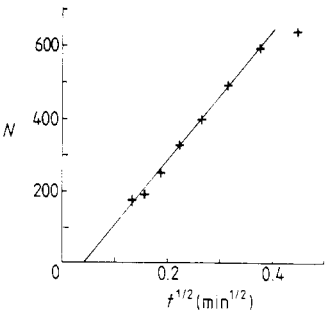

Figure 15. Number of extrema in a given area versus $t^{-1/2}$ for oilscapes.

and the proportion of these will increase with time. The reason for the divergence of the first (highest N) point is less clear, but may arise from nonlinear effects at high height to thickness ratio.

As explained in § 2.4, the time variation of surface heights, and hence of slopes and curvatures, depends on the exponent μ of the power-law variation of $P(s, 0)$ with s, which is not theoretically predictable. An experimental study has been attempted, using the curvatures and slopes of the oilscapes.

As indicated above, the time variation of curvatures may be studied by use of the chicken-wire caustics. The slide holding of oil film was traversed away from the camera (now used simply as a magnifying viewer) by a micrometer, which also operated the pen of a computer-timed pen recorder. The result, figure 15, shows that the focal distance varies linearly with time, which on the basis of equation (25) suggests that μ has the value 2. For distances greater than 25 mm (the three circled points) the camera was moved back, with position by millimetre scale and time by stopwatch. The relative unreliability of these points however arises mainly from the increasing depth of focus of the chicken-wire, which is a consequence of scaling associated with a cusp diffraction catastrophe (Berry and Upstill 1980): it can be shown that the ratio (depth of focus)/(focal distance) increases as $t^{1/4}$.

It may be noted that the line of figure 15 does not pass through the origin. This is to be expected since the initial spatial frequency will not be infinite but more probably of the order of the inverse of the mean film thickness.

The linear variation of focal distance with time corresponds to $\mu = 2$ and so, by

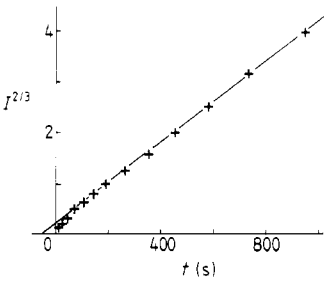

Figure 16. (Intensity)$^{2/3}$ versus time at the centre of the far-field distribution for an oilscape.

equation (24), implies a $t^{-3/4}$ variation of slopes (and also, by equation (20), a $t^{-1/2}$ variation of heights.) Two experiments were conducted to study the slopes. Firstly a laser beam, 10 mm diameter at the film, was arranged to focus (with the film absent) on a calibrated silcon photodiode 1 m behind this position. With the film in place the light is spread in an approximately Gaussian distribution, the radius of which is proportional to the average surface slopes. A $t^{-3/4}$ variation of slope would cause the central light intensity I to vary as $t^{3/2}$. Figure 16 shows $I^{2/3}$ versus t, confirming a linear variation. This method of plotting was chosen in the expectation that there might be a departure from the law at small times, and that the line would not pass precisely through the origin.

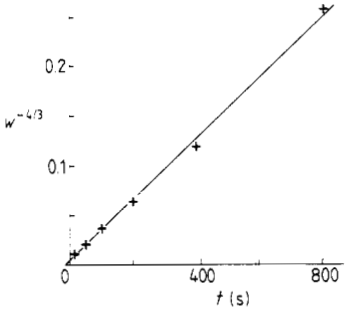

Figure 17. $w^{-4/3}$ versus time, where w is the e^{-1} half-width of the intensity distribution from an oilscape.

The second experiment involved traversing the photocell rapidly across the illuminated region, using a pen recorder to record intensity versus photocell position, and hence measure directly the variation in width of this region with time. Figure 17 shows $w^{-4/3}$, where w is the half-width of the distribution at e^{-1} intensity ratio, versus time. Again the linear variation is confirmed, and again there is a slight offset from the origin. The intensity distributions were found to be approximately but not exactly Gaussian. The slightly more leptokurtic experimental distribution probably results from variations of mean film thickness. If the film is made very thin and the height variations are comparable to the light wavelength, some light is directly transmitted and a bright central spot appears. The film thickness and height variations used in the experiment were, however, large enough to prevent this.

As already stated, the observed time variations of slopes and curvatures, together with the analysis of § 2.4, imply an initial power spectrum $P(s, 0)$ proportional to s^2, at least over a range of scales betwen the 50 μm thickness and several cm extent of the film. At later times the spectrum $P(s, t)$ would then be proportional to $s^2 \exp(-s^4 t)$, consistent with the band-limited appearance of the oilscapes, mentioned previously. The exponent $\mu = 2$ corresponds to a surface quite different from the negative values characteristic of natural fractals (Mandelbrot 1982), and indeed nothing in the rolling process by which oilscapes are created could give the large relative low-frequency content possessed by fractals. The large relative content of *high* frequencies for the oilscapes must be connected with 'unsticking' at the moment they are formed, but why this should lead to $\mu = 2$ (rather than some other positive value) is not clear to us (it might be related to the fact that s^2 is the first term of a Taylor expansion for an analytic $P(s, 0)$ without zero-frequency content).

4. Conclusions

Starting from the profile equation (5), simple solutions for two and three-dimensional oil hills have been derived. The experiments confirm that a point or line disturbance gives rise to recognisable combinations of these solutions. and that their profiles and time development agree with the theory.

Apart from their slightly wavy edges, these hills are the simplest localised deformations of a flat surface, and produce correspondingly simple light caustics.

The theory also covers a random wave distribution, giving rise to random oilscapes having stable statistics and predictable increase of lateral scale with time. These are also readily produced experimentally and the lateral time variation is confirmed. The contrast between these 'rough' liquid surfaces and rough solid surfaces, which is very evident in the interferograms, appears also in the form of the power spectrum which is implied by the observed slope and curvature variations.

Acknowledgments

The authors wish to thank: Dr F J Maillardet and staff of the Mechanical and Production Engineering Department of Brighton Polytechnic (of which Mr Tanner was formerly a member) for provision of darkroom and other facilities, and Dr D J Dingley, of Bristol University, for coating of semi-reflecting plates.

This research was not supported by any military agency.

Appendix 1: Mathematical aspects of oil hills

A convergent power series for the k-hill profile (10) can be obtained by substituting the power series for the Bessel function and then using the duplication formula for gamma functions (Abramowitz and Stegun 1964). The result is

$$Z_k(\rho) = \tfrac{1}{2}\sqrt{\pi}\left(\frac{\rho}{2}\right)^k \sum_{n=0}^{\infty} \frac{(-1)^n(\rho/2)^{2n}}{n!\Gamma(n/2 + k/2 + 1)}. \tag{A1.1}$$

This is a convenient representation if ρ is not large, and was employed in calculating figure 1(a).

Determining the asymptotic behaviour for large ρ involves two steps. First, the Bessel function is approximated by its large-argument asymptotic form (Abramowitz and Stegun 1964), to give

$$Z_k(\rho) \approx \mathrm{Re}\left(\frac{2}{\pi\rho}\right)^{1/2} \int_0^{\infty} \mathrm{d}\sigma\, \sigma^{(k+1/2)} \exp(-\sigma^4/4 + \mathrm{i}\rho\sigma) \exp[-\mathrm{i}\pi(k + \tfrac{1}{2})/2] \tag{A1.2}$$

Second, the integral is approximated by the method of steepest descent (Bender and Orszag 1978), the stationary point being that of the exponential (and not the factor $\sigma^{(k+1/2)}$, which lies at

$$\sigma_c = \rho^{1/3} \exp(\mathrm{i}\pi/6). \tag{A1.3}$$

Deformation of the integration contour so as to pass through this point then leads to

$$Z_k(\rho) \approx \frac{2}{\sqrt{3}}\rho^{(k-2)/3}\exp(-\rho^{4/3}/8)\cos\left(\frac{3\sqrt{3}}{8}\rho^{4/3} - \frac{\pi}{3}(k+1)\right)(\rho \to \infty). \tag{A1.4}$$

This formula will be a good approximation provided $\rho \gg (k+1)^{3/4}$, as can be shown by analysis of the condition for the validity of the Bessel approximation that led to equation (A1.2).

The decaying oscillations described by equation (A1.4) are of mathematical interest but are not easy to observe because they correspond to very small surface deformations. In practice it is sufficient to approximate the k-hills by Gaussians fitted to the first two non-zero derivatives. Inspection of equation (A1.1) shows that these Gaussians are

$$\left.\begin{aligned} Z_k(\rho) &\approx \frac{\Gamma[(k+1)/2]}{2k!}\rho^k \exp(-\rho^2/2w_k^2) \\ \text{where} \\ w_k^2 &= \frac{(k+1)\Gamma[(k+1)/2]}{\Gamma(k/2+1)}. \end{aligned}\right\} \tag{A1.5}$$

In Appendix 3 these approximations will be used in calculations of optical caustics produced by oil hills.

The k-hill and its corresponding Gaussian are also related by an exact formula, namely

$$\tfrac{1}{2}\sqrt{\pi}\rho^k \exp(-\rho^2/2) = \int_0^\infty \mathrm{d}\sigma\, \sigma^{k+3}\exp(-\sigma^4/4)Z_k(\sigma\rho) \tag{A1.6}$$

whose correctness can be confirmed by substituting the power series (A1.1). This representation of a Gaussian as a superposition of k-hills provides the following interesting alternative to the fundamental Fourier decomposition (6) for determining the evolution of hills whose initial profile is Gaussian. We begin by noting that any superposition of oil hills (equation (8)) corresponding to pin-pricks at $\boldsymbol{r} = 0$ at different times will also be a solution of the profile equation (5). Restricting ourselves for simplicity to the case of azimuthal isotropy ($k = 0$) we can write such a superposition as

$$z(r,t) = \frac{ah}{\tau}\int_{-\infty}^{t} \mathrm{d}t'\left(\frac{\tau}{t-t'}\right)^{1/2} Z_0\left(\frac{r\tau^{1/4}}{h(t-t')^{1/4}}\right) f(t') \tag{A1.7}$$

for any source history $f(t')$. If now we choose

$$f(t') = \frac{r_0^4}{h^4 2\sqrt{\pi}}\left(\frac{-t'}{\tau}\right)^{-3/2}\exp\left(\frac{\tau r_0^4}{4t'h^4}\right) \tag{A1.8}$$

and change to the new integration variable

$$\sigma \equiv r_0\tau^{1/4}/(t-t')^{1/4}h$$

we obtain

$$z(r,t) = \frac{2ah}{\sqrt{\pi}}\int_0^{r_0/h(\tau/t)^{1/4}} \frac{\mathrm{d}\sigma\,\sigma^3\exp[-\sigma^4/4(1-th^4\sigma^4/\tau r_0^4)]}{(1-th^4\sigma^4/\tau r_0^4)^{3/2}} Z_0(r\sigma/r_0). \tag{A1.9}$$

The initial profile that generates the evolving hill can be identified by equation (A1.6) as

$$z(r, 0) = ah \exp(-r^2/2r_0^2) \tag{A1.10}$$

and is indeed a Gaussian. The profile into which equation (A1.9) eventually develops can be identified by noting that as $t \to \infty$ the integral is dominated by its upper limit at which the factors involving σ^4 are singular. Expansion about this singularity leads after some calculation to

$$z(r, t \to \infty) = \frac{ar_0^2}{h}\left(\frac{\tau}{t}\right)^{1/2} Z_0(\rho). \tag{A1.11}$$

(it can be confirmed that this hill has the same volume as the initial Gaussian.)

Appendix 2: Mathematical aspects of oil ridges

A convergent power series for the j-ridge profile (equation (15)) can easily be obtained as

$$\left.\begin{aligned} Z_j(\xi) &= (-1)^{j/2} 2^{(j-3)/2} \sum_{m=0}^{\infty} (-2)^m \frac{\Gamma[\frac{1}{4}(j+2m+1)]\xi^{2m}}{(2m)!} && (j \text{ even}) \\ &= \xi(-1)^{(j+1)/2} 2^{(j/2)-1} \sum_{m=0}^{\infty} \frac{(-2)^m \Gamma[\frac{1}{4}(j+2m+2)]\xi^{2m}}{(2m+1)!} && (j \text{ odd}) \end{aligned}\right\} \tag{A2.1}$$

and is a convenient representation when ξ is not large.

When ξ is large (j fixed), the method of steepest descent can be employed, exactly as for the k-hill (A1.2), to yield

$$z_j(\xi) \simeq \left(\frac{2\pi}{3}\right)^{1/2} \xi^{(j-1)/3} \exp(-3\xi^{4/3}/8) \cos\left(\frac{3\sqrt{3}}{8}\xi^{4/3} + \frac{\pi}{6}(4j-1)\right) (\xi \to \infty) \tag{A2.2}$$

When j is large (ξ fixed), steepest descent can again be employed, but now the factor σ^j in equation (15) must be included, so that what has to be considered is the exponent

$$j \ln \sigma - \sigma^4/4 + i\xi\sigma$$

whose stationary point for large j lies at

$$\sigma_c \approx j^{1/4} + i\xi/4j^{1/2} (j \to \infty). \tag{A2.3}$$

Application of steepest descent now gives

$$\left.\begin{aligned} Z_j(\xi) \approx \left(\frac{\pi}{2}\right)^{1/2} & j^{(j-1)/4} \exp(-j/4) \exp(-\xi^2/8j^{1/2}) \\ & \times \begin{cases} (-1)^{j/2} \cos j^{1/4}\xi & (j \text{ even}) \\ (-1)^{(j+1)/2} \sin j^{1/4}\xi & (j \text{ odd}) \end{cases} \end{aligned}\right. \tag{A2.4}$$

(It is possible to combine equations (A2.2) and (A2.4) into a more comprehensive asymptotic formula, but this is complicated and we will not present it.)

To explore the evolution of initially Gaussian ridges, i.e.

$$z(x, 0) = ah \exp(-x^2/2x_0^2) \tag{A2.5}$$

we simply take the Fourier transform and employ the fundamental solution (equation (6)), to get

$$z(x,t) = \frac{ahx_0}{\sqrt{2\pi}} \int_{-\infty}^{\infty} \mathrm{d}s \exp\left(\frac{-s^2x_0^2}{2} + \mathrm{i}sx - \frac{s^4h^4t}{4\tau}\right) \tag{A2.6}$$

For large t, the quartic term in the exponent dominates the quadratic one, leading with the aid of equation (15) to the eventual profile

$$z(x, t \to \infty) = ax_0\left(\frac{\tau}{t}\right)^{1/4} \sqrt{\left(\frac{2}{\pi}\right)} Z_0(\xi). \tag{A2.7}$$

Appendix 3: Far-field caustics from oil hills

Light transmitted through an oil hill will be focused because of refraction by its curved profile (Berry and Upstill 1980). In space the focal singularities take the form of caustic surfaces. In the far field the caustic $\mathscr{C}$ in the plane of directions $\boldsymbol{R} \equiv (X, Y)$ is a line given parametrically by

$$\boldsymbol{R}(p,t) = \nabla z(\boldsymbol{r}(p), t) \tag{A3.1}$$

where $\boldsymbol{r}(p)$ is the line $\mathscr{L}$ of zero Gaussian curvature on the hill, parameterised by p. $\mathscr{L}$ is the set of points satisfying

$$z_{xx}z_{yy} - (z_{xy})^2 = 0 \tag{A3.2}$$

where subscripts denote derivatives.

Catastrophe theory (Berry and Upstill 1980) predicts that for almost all hills $\mathscr{C}$ will consist of smooth curves ('fold' caustics) joining in pairs at cusp points. For particular hills, higher singularities occur, the simplest of which are *umbilic foci*, originating on the hill from the isolated points $\boldsymbol{r}$ where the two principal curvatures are equal, i.e.

$$z_{xx} - z_{yy} = z_{xy} = 0.$$

When combined with equation (A3.2) this shows that the condition for an umbilic focus to occur in the far field is that all three second derivatives of z vanish.

An important case where such a far-field umbilic occurs is the scaling hill $z_1(\boldsymbol{r}, t)$ defined by equations (8) and (10). This has the form

$$z_1(\boldsymbol{r}) = xF(r) \tag{A3.3}$$

where $F(r)$ is an even function and where the t-dependence is no longer indicated. Near the origin,

$$z_1(r) \approx xF(0) + \tfrac{1}{2}x(x^2 + y^2)F''(0) \tag{A3.4}$$

whose second derivatives at $r = 0$ do indeed all vanish.

To determine whether this umbilic is elliptic or hyperbolic we employ the discriminant of Berry and Hannay (1977).

If

$$\left.\begin{aligned} C \equiv 4(z_{xxx}z_{xyy} - z_{xxy}^2)(z_{xxy}z_{yyy} - z_{xyy}^2) - (z_{xxx}z_{yyy} - z_{xxy}z_{xyy})^2 \\ > 0 \text{ then elliptic} \\ < 0 \text{ then hyperbolic.} \end{aligned}\right\} \tag{A3.5}$$

From equation (A3.4), the discriminant at the umbilic has the value

$$C = -12[F''(0)]^4 \tag{A3.6}$$

indicating that the umbilic is *hyperbolic*. To obtain the explicit form of $\mathscr{C}$ near the umbilic focus, it is first necessary to find the form of $\mathscr{L}$ near the umbilic point on the hill; substitution of equation (A3.4) into (A3.2) gives this as

$$y^2 = 3x^2. \tag{A3.7}$$

Now equation (A3.1) with p taken proportional to x gives $\mathscr{C}$ as

$$X(p) = F(0) - 2p^2 \qquad Y(p) = \pm 2p^2/\sqrt{3} \tag{A3.8}$$

where the fact that $F''(0) < 0$ has been used. These equations yield the prediction that the caustic lines make an angle of 60° where they meet at the umbilic focus.

To see the full unfolding of the hyperbolic umbilic catastrophe in the far field is necessary to perturb z_1. The obvious perturbation is the isotropic hill z_0. In order to get analytical formulae describing the global caustic from the perturbed hills we approximate z_0 and z_1 by Gaussians as in equation (A1.5), and in addition set the widths w_0 and w_1 equal to each other (the correct ratio would be $w_0/w_1 = \frac{1}{2}\sqrt{\pi} = 0.886$). Thus the caustic to be studied is that from

$$z(\boldsymbol{r}) = (x + a)\exp(-r^2/2) \tag{A3.9}$$

where a is the perturbing parameter. This leads via equation (A3.2) to the following formula for $\mathscr{L}$:

$$y(x) = \pm\left(\frac{(x+a)^2(1-x^2) + 2x(x+a)}{1 + (x+a)^2}\right)^{1/2}. \tag{A3.10}$$

The caustic now follows from equation (A3.1) as

$$\begin{aligned} X(x) &= [1 - x(x+a)]\exp[-\tfrac{1}{2}(x^2 + y(x)^2)] \\ Y(x) &= \pm(x+a)y(x)\exp[-\tfrac{1}{2}(x^2 + y(x)^2)] \end{aligned} \tag{A3.11}$$

where x plays the role of the parameter p.

Figure 7(*d–f*) show this caustic for three values of a. The characteristic 'teardrop in a loop' shapes unfold from the hyperbolic umbilic singularity at $a = 0$ (pure z_1) towards the focal point in a circle at $a = \infty$ (pure z_0). (The focal point for $a = \infty$ is an artefact of the Gaussian approximations; for the true asymptotically rippling oil hills the teardrop would shrink into a complicated ring structure rather than a point.)

References

Abramowitz M and Stegun I A 1964 *Handbook of Mathematical Functions* (Washington, DC: National Bureau of Standards)

Bender C M and Orszag S A 1978 *Advanced Mathematical Methods for Scientists and Engineers* (New York: McGraw-Hill)

Berry M V and Hannay J H 1977 *J. Phys. A: Math. Gen.* **10** 1809–21

Berry M V and Upstill C 1980 *Prog. Optics* **18** 257–346

Gradshteyn I S and Ryzhik I M 1965 *Tables of Integrals, Series and Products* (New York: Academic Press)

Jeffreys E 1930 *Proc. Camb. Phil. Soc.* **6** 204–5

Longuet-Higgins M S 1957a *Phil. Trans. R. Soc.* A **249** 321–87

—— 1957b *Phil. Trans. R. Soc.* A **250** 157–74

Mandelbrot B B 1982 *The Fractal Geometry of Nature* (San Francisco: Freeman)
Tanner L H 1977 *J. Phys. E: Sci. Instrum.* **10** 1019–28
—— 1979 *J. Phys. D: Appl. Phys.* **12** 1473–85
—— 1980 *J. Phys. D: Appl. Phys.* **13** 1633–41
—— 1981 *Optics and Lasers in Engineering* **2** 105–18
—— 1982 *Optics and Lasers in Engineering* **3** 101–10
Tanner L H and Blows L G 1976 *J. Phys. E: Sci. Instrum.* **9** 194–202